



Article

Modification of Cycle Life Model for Normal Aging Trajectory Prediction of Lithium-Ion Batteries at Different Temperatures and Discharge Current Rates

Xinyu Jia ¹, Caiping Zhang ¹, Leyi Wang ², Weige Zhang ¹ and Linjing Zhang ^{1,*}

¹ National Active Distribution Network Technology Research Center (NANTEC), Beijing Jiaotong University, Beijing 100044, China; xinyu.jia@bjtu.edu.cn (X.J.); zhangcaiping@bjtu.edu.cn (C.Z.); wgzhang@bjtu.edu.cn (W.Z.)

² Department of Electrical & Computer Engineering, Wayne State University, Detroit, MI 48202, USA; lywang@wayne.edu

* Correspondence: lj.zhang@bjtu.edu.cn

Abstract: Battery life is of critical importance for the reliable and economical operation of electric vehicles (EVs). Normal aging accounts for more than 80% of the battery available cycle range. Accurate and robust battery life models of normal aging are essential for battery health management systems and life evaluation before accelerated aging. Capacity recovery, test errors and accelerated aging all affect life model building during normal aging. Therefore, this paper proposes an improved life model based on wavelet transform (WT) signal processing to accurately predict the decline trend of the battery in the normal aging stage. In this paper, the capacity recovery, test noise and capacity diving in the aging trend are effectively removed by wavelet transform. We obtained an optimized life model through the analysis of the model structure and the analysis of the parameter sensitivity of the life model. The particle swarm algorithm (PSO) is employed to identify the parameters of the empirical models with the normal aging data extracted by the WT. Through verification, it is found that the modified cycle life model proposed in this paper can accurately predict the normal aging trajectory of batteries under different discharge rates and temperatures. The prediction error of the improved life model for normal aging is 1.09%.

Keywords: normal aging; battery aging model; aging model modification; wavelet transform



Citation: Jia, X.; Zhang, C.; Wang, L.; Zhang, W.; Zhang, L. Modification of Cycle Life Model for Normal Aging Trajectory Prediction of Lithium-Ion Batteries at Different Temperatures and Discharge Current Rates. *World Electr. Veh. J.* **2022**, *13*, 59. <https://doi.org/10.3390/wevj13040059>

Academic Editor: Haijun Ruan

Received: 3 March 2022

Accepted: 25 March 2022

Published: 28 March 2022

Publisher's Note: MDPI stays neutral with regard to jurisdictional claims in published maps and institutional affiliations.



Copyright: © 2022 by the authors. Licensee MDPI, Basel, Switzerland. This article is an open access article distributed under the terms and conditions of the Creative Commons Attribution (CC BY) license (<https://creativecommons.org/licenses/by/4.0/>).

1. Introduction

In recent years, Li[Ni_{0.5}Co_{0.2}Mn_{0.3}]O₂ (NCM) batteries have been widely used in electric vehicles (EVs) and hybrid electric vehicles (HEVs) due to their extended cycle life and high energy density [1,2]. Battery life, which is of significance for reliable and economical operation of electric vehicles, usually includes calendar life and cycle life [3]. The degradation of battery consists of normal degradation and accelerated aging. The normal degradation is caused by the continuous growth of solid electrolyte interface (SEI). The trend of normal degradation is approximately linear [4]. The degradation of battery may lead to safety problems and reduce ranges of EVs [5–7]. Therefore, it is necessary to predict the battery ageing trajectory accurately.

Many life prediction methods for lithium-ion batteries have been proposed [8], which can be divided into two types: data-driven methods and model-based methods [9,10]. Data-driven methods for battery life prediction include support vector machine (SVM) [11], sparse Bayesian predictive modeling (SBPM) [12], long short-term memory (LSTM) recurrent neural network (RNN) [13]. Data-driven methods can predict RUL well without considering aging mechanism [14,15]. However, the data-driven methods can not consider the impact of working conditions, such as: discharge current and temperature [8]. Compared with data-driven life prediction method, model-based life prediction method can involve the impact of the working conditions, degradation mechanisms and calendar life.

Bloom et al. [16] studied the calendar life and cycle life of lithium-ion batteries, and found that, according to the solid electrolyte interface (SEI) layer growth, the calendar and cycle lives of a battery followed a cycle number to the power of $1/2$ ($n^{1/2}$) and Arrhenius kinetics. The common form of battery cycle life model is the cycle number to the power of $1/2$ based on the SEI growth phenomenon [17,18]. In addition to the power of $1/2$, the double exponential cycle life model is another common life model which describes the time dependency [19]. The cycle life model agreed well with the experimental data but featured a much higher power law factor (1.3) compared to the value of 0.5 associated with the general $t^{1/2}$ rule based on the rate of solid electrolyte interphase (SEI) growth [18]. Arrhenius equation can be used to improve the extrapolation ability of the life model under various temperatures [20]. A life model which describes capacity fade and resistance increase as a function of the influencing stress factors and battery charge throughput was proposed [21]. John Wang et al. [22] proposed a cycle life model with an Arrhenius correlation and the exponential dependence of the current rate. Johannes Schmalstieg et al. [23] created a cycle life model taking cycle depths and mean state of charge (SOC) into account. Pecht Michael et al. [24] developed an empirical accelerated degradation model that can describe the two-stage capacity fade process. The double exponential cycle life model was improved for the accelerated aging [25]. Stefan Kabitz et al. [17] built a life model by combining a calendar life model and a cycle life model. In addition to the empirical model considering the impact of the cycle time and the operation conditions, researchers also built the life model based on the impedance spectroscopy [26], physics-based single-particle model [27], coulombic efficiency [28] and lithium plating [29].

Compared with data-driven life prediction method, model-based life prediction method can involve the impact of the working conditions, degradation mechanisms and calendar life. Along with battery ageing, the capacity recovery and accelerated aging will happen [24,30]. The accelerated aging can be caused by the accelerated loss of the cathode material and the lithium ion [31–33]. Before accelerated ageing, battery ageing trajectory is normal ageing which is approximately linear. After accelerated ageing, the ageing trajectory becomes nonlinear. Accelerated ageing, capacity recovery and test noise [29,34] will reduce the life model accuracy for normal ageing. In order to overcome the negative impacts of accelerated ageing, capacity recovery and test noise on the life model of normal ageing, we propose wavelet transform-based cycle life model for normal ageing. The main contributions of this paper are summarized in the following: battery aging cycle tests under different temperatures and discharge current were performed. The capacity recovery, accelerated ageing and test noise are comprehensively studied in this paper. Due to the excellent denoise ability and filterability, the wavelet transform is proposed to extract the main normal ageing trajectory for life model raining. The parameters sensitivity was performed using the statistical Multi-Parameter Sensitivity Analysis (MPSA) to find the crucial parameters for normal ageing and provide guidance for life model improvement. A modified empirical life model was proposed based on the MPSA and WT for normal ageing [35].

The remaining structure of this paper is arranged as follows: in Section 2, the experimental test and results of the battery is introduced. Section 3 introduces the extraction of normal ageing trajectory based on wavelet transform. Section 4 presents the modification of the life model for normal ageing trajectory prediction. Section 5 summarizes the conclusions of this paper.

2. Cycle Life Experiments and Results

2.1. Cycle Life Test

In this work, two types of NCM batteries were tested under different temperatures and discharge current rates. The aging dataset has been published in the IEEE DataPort, DOI: 10.21227/gnst-kz81 for the battery aging study. The battery cycle life experiments and the reference performance test (RPT) were performed to investigate NCM battery aging characteristics. The RPT was performed periodically during the cycle life test. The first

kind of NCM battery is marked as Battery I. The second kind of NCM battery is marked as Battery II. The detailed information of these two kinds of battery is listed in Table 1.

Table 1. Nominal specifications of the batteries.

Item	Battery I	Battery II
Cathode material	$\text{Li}[\text{Ni}_{0.5}\text{Co}_{0.2}\text{Mn}_{0.3}]\text{O}_2$	$\text{Li}[\text{Ni}_{0.6}\text{Co}_{0.2}\text{Mn}_{0.2}]\text{O}_2$
Anode material	Graphite	Graphite
Nominal capacity	114 Ah	36 Ah
Charging cut-off voltage	4.25 V	4.15 V
Discharging cut-off voltage	2.8 V	2.5 V
Shape	prismatic	pouch

The cycle temperatures and discharge current rate are shown in Tables 2 and 3. The batteries were placed in the environmental chambers during charging and discharging to achieve the target temperatures. There are two batteries for each condition measurement. Multiple constant currents charging protocol is employed for Battery I, that is, 1.2 C to 3.791 V, 0.87 C to 4.114 V, 0.33 C to 4.25 V, 0.1 C to 4.25 V, and 0.05 C to 4.25 V. The protocol for Battery II is constant-current constant voltage (CCCV), charged at 1 C to 4.15 V and charged at a constant voltage 4.15 V to 0.05 C. The charge profile is provided by battery manufacturer. The batteries are placed in the biochemical incubators during charging and discharging so that the battery test temperature can be controlled during tests. Additionally, the battery test temperature flows around the set temperature, and temperature fluctuation range is within 2 °C.

Table 2. Cycle life conditions of Battery I.

Condition Number	Cycle Temperature	Discharge Current Rate
1	25 °C	1 C
2	35 °C	1 C
3	45 °C	1 C
4	50 °C	1 C
5	55 °C	1 C
6	25 °C	0.5 C
7	25 °C	1 C
8	25 °C	1.5 C
9	25 °C	2 C

Table 3. Cycle life conditions of Battery II.

Condition Number	Cycle Temperature	Discharge Current Rate
10	25 °C	1 C
11	35 °C	1 C
12	45 °C	1 C
13	25 °C	1 C
14	25 °C	1.5 C
15	25 °C	2 C
16	35 °C	1.5 C
17	35 °C	2 C

During the battery cycle life tests, the RPT was periodically conducted at 25 °C. The battery RPT included a nominal capacity test, a hybrid pulse power characterization (HPPC) test, and a charge and discharge test at small current density of 1/20 C. There were three charge and discharge cycles for the battery nominal capacity test by following the charging strategy provided by the battery manufacturer, and a discharge current rate of 1/3 C. The capacity measured at the third cycle was identified as the battery nominal

capacity. The charge and discharge capacity at 1/20 C were considered as the maximal available capacities of the battery. A HPPC test was conducted to obtain the internal resistance of the battery at different SOC.

2.2. Cycle Life Test Results

In this paper, the capacity retention rate is used to describe the degradation of the battery capacity. The capacity retention rate C_{re} is calculated by Formula (1). The cumulative discharge ampere hour is calculated by Formula (2)

$$C_{re} = \frac{Q_n}{Q_{start}} \cdot 100\% \quad (1)$$

$$Ah_{throughput} = \sum_{n=1}^N Ah_{dis, n} \quad (2)$$

where Q_n is the actual capacity at n th cycle $Ah_{throughput}$. Q_{start} is the capacity at the initial cycle test. $Ah_{throughput}$ is the cumulative discharge ampere-hour from the first cycle to the N th cycle. n is the cycle number. $Ah_{dis, n}$ is the discharge ampere-hour at the n th cycle.

Figure 1a shows the capacity retention of Battery I at 25–55 °C and 0.5–2 C. The degradation characteristics of Battery I at 25–55 °C are normal aging (approximately linear). The capacity degradation speed shows a significant increase after 100,000 $Ah_{throughput}$ at 0.5 C and 1 C, while the capacity decay is slower at 1.5 C and 2 C. It is noted that there are many obvious data noises for battery cycle life tests. The data noises are caused by the test error and the capacity recovery during RPT. The capacity recovery phenomenon may influence the battery life prediction [34,36]. Figure 1b shows the capacity retention of Battery II with $Ah_{throughput}$ at 25–45 °C and at 1–2 C. The Battery II experienced obvious accelerated aging during cycling. The aging process of Battery II included normal aging stage and accelerated aging stage. During the normal fade stage, the capacity of Battery II declined faster at 35 °C and 45 °C than that at 25 °C. However, the accelerated aging point appeared earlier at 25 °C and 45 °C than the Battery II at 35 °C. The cycle life of Battery II was longest at 35 °C. For the discharge current rate under 1–2 C, the capacity degradation speeds of Battery II were similar during the normal stage. The accelerated aging point arose earlier at 2 C rate.

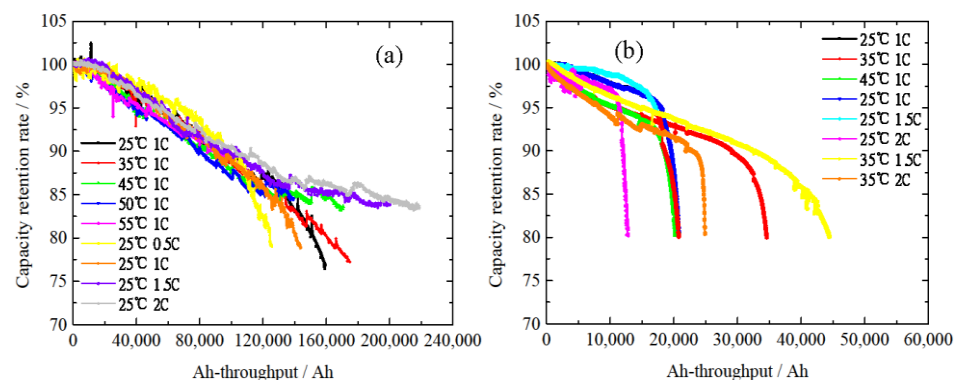


Figure 1. (a) Capacity degradation of Battery I; (b) capacity degradation of Battery II.

According to our experiment results, Battery I, with high energy density, has a longer life than Battery II. The normal degradation stage of Battery I is longer than that of Battery II. It seems that the temperature and discharge current rate only have an impact on the accelerated degrading point, and they have little impact on the battery degradation during normal stage. Above all, the degradation data includes the test noises, the capacity recovery and capacity drop variations. The degradation data need to be processed before identification of the empirical model parameters. In the later discussion, the cycle life test data of Battery I are marked as Dataset I, and as Dataset II for the test data of Battery II.

3. Normal Aging Trajectory Acquisition Based on Wavelet Transform

3.1. Wavelet Transform Method

Suppose $\psi(t)$ is a basic wavelet. The wavelet analysis function is obtained by scaling and translation of the $\psi(t)$:

$$\psi_{a,b}(t) = |a|^{-\frac{1}{2}} \cdot \psi\left(\frac{t-b}{a}\right) \quad (3)$$

where a and b are the expansion and contraction factors, respectively. The continuous wavelet transform is defined as:

$$W_f(a,b) = f * \psi_{a,b}(t) = \frac{1}{\sqrt{a}} \int_{-\infty}^{+\infty} f(t) \cdot \psi_{a,b}(t) dt \quad (4)$$

where $W_f(a,b)$ is a function of the scale parameter a and the spatial position b . The larger the scale parameter, the more details you can observe. After obtaining the wavelet coefficients at different scales, the wavelet coefficients of the noisy signal are processed, and then the wavelet coefficients generated by reducing or eliminating the noise are subjected to wavelet inverse transformation to obtain the denoised signal $f(t)'$. After obtaining the denoised signal, we calculate the average aging speed with denoising and without denoising. The change of the average cycle degradation speed Δv is used to evaluate the denoising effect with the wavelet transform.

$$v_1 = Q_{i+1} - Q_i \quad (5)$$

$$v_{\text{average1}} = \frac{1}{N} \cdot \sum_1^N v_1 \quad (6)$$

$$v_2 = Q'_{i+1} - Q'_i \quad (7)$$

$$v_{\text{average1}} = \frac{1}{N} \cdot \sum_1^N v_1 \quad (8)$$

$$v_{\text{average2}} = \frac{1}{N} \cdot \sum_1^N v_2 \quad (9)$$

$$\Delta v = (v_{\text{average1}} - v_{\text{average2}}) / v_{\text{average1}} \cdot 100 \quad (10)$$

where Q_i is the capacity retention before denoising and i is the cycle number. v_1 is the aging speed before denoising. v_{average1} is the average aging speed before denoising. N is the total cycle number. Q'_i is the capacity retention after denoising, and i is the cycle number. v_2 is the aging speed after denoising. v_{average2} is the average aging speed after denoising.

After WT, for accelerated aging batteries, we removed aging trajectory after the aging speed v_2 exceeded 0.05% to obtain the normal aging process before accelerated aging.

3.2. Normal Aging Trajectory Acquisition Results

Figure 2 shows the change of the maximal available capacity and cycle capacity of Battery I upon cycling. The retention rate of the maximal available capacity can be used as the indicator of the irreversible capacity loss [1]. In our experiments, low current density $C/20$ was applied to accurately obtain the maximal available capacity. As shown in Figure 2, even though there is capacity recovery at the cycle capacity degradation curve, the degradation trend of the cycle capacity and the maximal available capacity are consistent and similar to each other. Therefore, the capacity recovery does not have a great impact on the battery aging. In addition to the capacity recovery, there are some noises in the cycle life degradation curve. The noises from capacity recovery and the cycle life tests are similar.

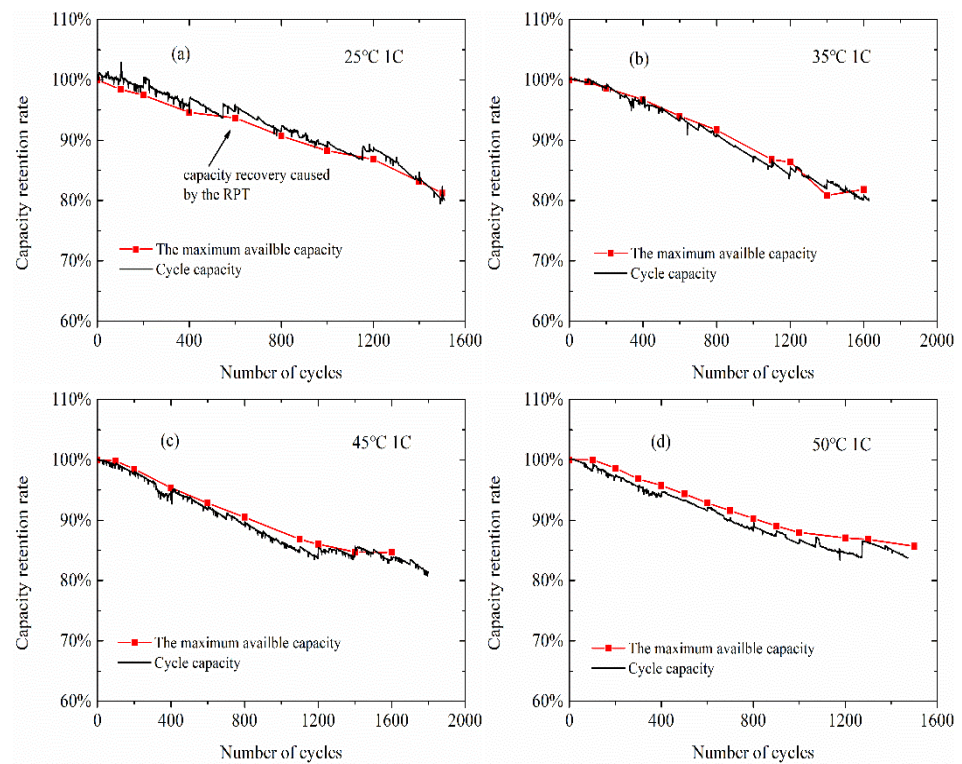


Figure 2. Comparison of the maximal available capacity and the cycle capacity of Battery I at different temperatures: (a) 25 °C, (b) 35 °C, (c) 45 °C and (d) 50 °C.

Generally, the appropriate wavelet function, the threshold estimation method, the decomposed number and the denoising method can be adopted to eliminate the data test noise, capacity recovery and capacity drop. The common wavelet functions include Haar wavelet, Daubechies (dbN) wavelet and SymletsA (symN) wavelet. The threshold estimation methods include sqtwolog, rigrsure, heursure and minimaxi. The denoising methods mainly contain two methods: hard and soft thresholding. The results of wavelet transform on the Dataset I are listed in the Table 4.

Table 4. The effects of eliminating the data test noise and capacity recovery by wavelet transform.

Wavelet Function	Decomposed Number	Denoising Method	Threshold Estimation Method	Δv
Haar	3	s	minimaxi	58–78%
Haar	3	h	minimaxi	52–77%
Haar	4	s	minimaxi	68–87%
db4	3	s	minimaxi	54–70%
db4	4	s	minimaxi	66–87%
db4	3	s	heursure	43–70%
db4	4	s	heursure	43–87%
db4	4	h	heursure	11–86%
db4	5	s	heursure	48–89%
db4	5	h	heursure	20–84%
sym4	4	s	heursure	44–87%
sym4	3	s	sqtwolog	65–80%

According to the Table 4, it can be observed that the effect of the removal of the data test noise and the capacity recovery do not improve with the decomposed number increasing from 3 to 5. The optimum decomposed number for denoising is 4. For the threshold estimation methods, both minimaxi and sqtwolog are better than the heursure method.

The soft denoising method is superior to the hard one in eliminating the noises of Dataset I. Finally, the db4 wavelet function, mimimaxi threshold estimation, soft denoising method and four decomposed numbers are selected to remove the data test noises and capacity recovery. The denoising results are shown in Figures 3 and 4. The capacity recovery and test noise reduce by 66–81% for Dataset I. The capacity drop of Dataset II is also eliminated. Therefore, the data denoising with the selected wavelet transform demonstrates good improvement in the removing effect of the data test noise, capacity recovery and capacity drop. The denoised datasets by wavelet transform will be used to train and validate the life model for normal aging in the following section.

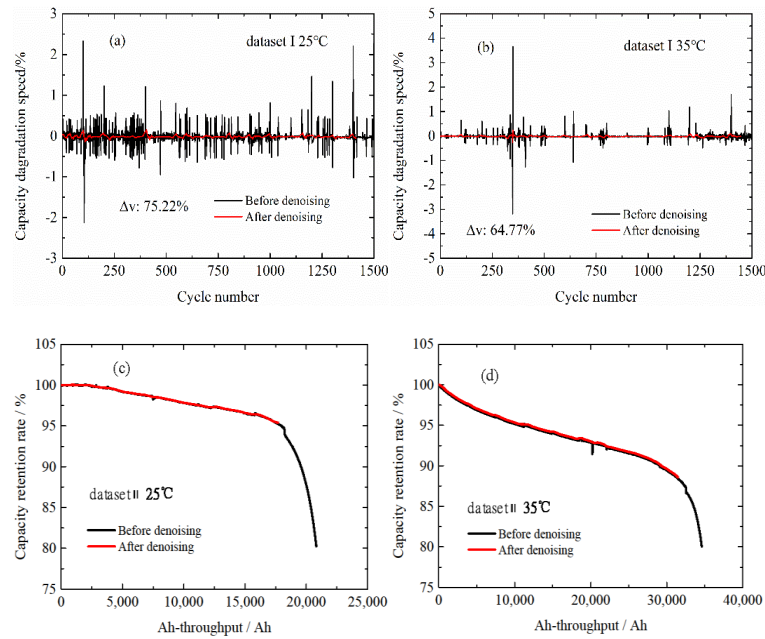


Figure 3. The denoising results with the wavelet transform: the per-cycle degradation speed of Dataset I at (a) 25 °C and (b) 35 °C; the removal of the capacity drop of Dataset II at (c) 25 °C and (d) 35 °C.

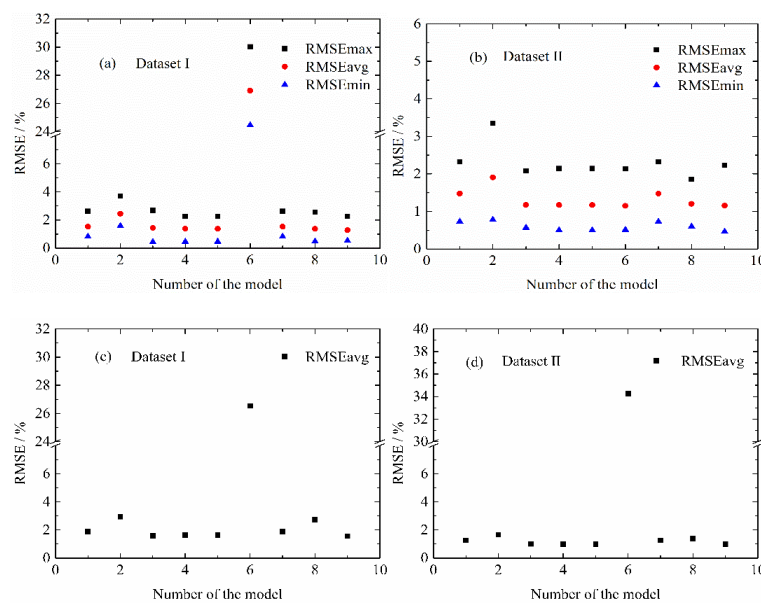


Figure 4. Prediction RMSE of the non-factor models for normal aging: (a) on the train dataset of Dataset I, (b) on the train dataset of Dataset II, (c) on the test dataset of Dataset I and (d) on the test dataset of Dataset II.

4. Modified Life Model for Normal Aging Trajectory Prediction

4.1. Introduction of the Empirical Models

Seventeen empirical models are selected from the reported literatures on the cycle life studies. These empirical models are listed in the Table 5. In these models, the Q_{loss} represents the loss of the capacity retention rate and the C represents the capacity retention rate. The n represents the cycle number, and the Ah represents the cumulative discharge capacity. Life model describes the dependency between the cycle number and the capacity. The cycle number can be measured by the cycle number or the cumulative discharge capacity. The cumulative discharge capacity means the total discharge capacity during cycle test. Compared with the cycle number, the cumulative discharge capacity is influenced by the cutoff voltage and depth of discharge, and it can reflect the influence of the cutoff voltage and depth of discharge on the battery aging to some extent. Therefore, in this paper, the cycle number is measured by the cumulative discharge capacity.

Table 5. The reported empirical models of battery cycle life.

Model	Model Parameter
1. $Q_{loss} = 1 - (a_1 * n^{0.5} + a_2)$	n is the cycle number; a_1, a_2 are the model parameters.
2. $C = 1 - a_1 * n^{0.5}$	n is the cycle number; a_1 is the model parameter.
3. $C = 1 - a_1 * n^{0.5} - a_2 * n$	n is the cycle number; a_1, a_2 are the model parameters.
4. $Q_{loss} = a_1 * n^{0.5} + a_2 * n + a_3$	n is the cycle number; a_1, a_2, a_3 are the model parameters.
5. $Q_{loss} = a_1 * n^{0.5} + a_2 * (n - N_0) + a_3$	n is the cycle number; a_1, a_2, a_3, N_0 are the model parameters.
6. $C = a_1 + a_2 * n + a_3 * n^2 + a_4 * n^3$	n is the cycle number; a_1, a_2, a_3, a_4 are the model parameters.
7. $C = a_1 + a_2 * n^{0.5}$	n is the cycle number; a_1, a_2 are the model parameters.
8. $Q_{loss} = 1 - (a_1 * \exp(a_2 * n) + a_3 * \exp(a_4 * n))$	n is the cycle number; a_1, a_2, a_3, a_4 are the model parameters.
9. $C = A * \exp\left(\frac{n}{t_1}\right) + y_0$	n is the cycle number; A, t_1, y_0 are the model parameters.
10. $Q_{loss} = B * \exp\left(\frac{-E_a}{R * T}\right) * n^z$	n is the cycle number; B and z are the model parameters; T is the absolute temperature; E_a is the active energy; and R is the universal gas constant.
11. $Q_{loss} = B * \exp\left(\frac{-E_a}{R * T}\right) * Ah^2$	Ah is the cumulative discharge capacity; B and z are the model parameters; T is the absolute temperature; E_a is the active energy; and R is the universal gas constant.
12. $C = 1 - d_{Tref} * \alpha \left(\frac{T - T_{ref}}{10}\right) * n^{0.5}$	T_{ref} is the reference temperature; n is the cycle number; d_{Tref} and α are model parameters; T is absolute temperature; and the T_{ref} is 40 °C in literature.
13. $C = A(I, T) * n^{B(I, T)}$ $A(I, T) = a * \exp\left(\frac{\lambda}{T}\right) + b * I^\beta + c$ $B(I, T) = l * \exp\left(\frac{\lambda}{T}\right) + m * I^n + f$	I is discharge current rate; T is absolute temperature; and $\alpha, \beta, l, \lambda, f, c$ are the model parameters.
14. $Q_{loss} = \alpha * \exp\left(\frac{k_3 * C_{rate} + k_4}{R * T}\right) * C_{rate}^\beta * n^\eta$	$\alpha, \beta, \eta, k_3, k_4$ are model parameters; R is the universal gas constant; n is the cycle number; T is absolute temperature; and C_{rate} is the discharge current rate.
15. $Q_{loss} = B * \exp\left(\frac{a + b * C_{rate}}{R * T}\right) * n^{0.55}$	a, b, B , are model parameters; R is the universal gas constant; n is the cycle number; T is absolute temperature; and C_{rate} is the discharge current rate.
16. $Q_{loss} = (a * T^2 + b * T + c) * \exp((d * T + e) * I_{rate}) * n$	T is the absolute temperature; n is the cycle number; I_{rate} is the discharge current rate; and a, b, c, d, e are the model parameters.
17. $Q_{loss} = (a * \exp(b * I) + c * \exp(d * I)) * \exp\left(\frac{e + f * I}{R * T}\right) * Ah^{0.55}$	I is the discharge current rate; R is the universal gas constant; T is the absolute temperature; Ah is the cumulative discharge capacity; and a, b, c, d, e, f are model parameters.

These seventeen empirical models can be classified into three types: the non-factors model [17,19,37–39], the single factor model [18,20] and the coupling factors model [22,40–43]. The non-factor empirical model has no parameters to reflect the impact of the operating conditions, such as temperature and discharge current rate. Models 1–9 in Table 5 represent the non-factor empirical models. These models do not consider any operating conditions, such as temperature or discharge current rate. Generally, the model with square root cycle number ($a \cdot time^{0.5}$) built for the SEI growth [14]. Based on such model, some researchers found there were other aging mechanisms in addition to the SEI growth, so the model was modified through combining the $a \cdot time^{0.5}$ with a normal function or enlarging the power of the model $a \cdot time^x$. In addition to the power function, the double exponential function (Model 8) is another non-factor empirical model, which is just based on the regression analysis of experiment data, and it does not represent any degradation mechanism.

The second kind of empirical model is the single factor model, which mainly considers the temperature factor. The single empirical model is built based on the non-factor empirical

model. The Arrhenius model is usually used to express the temperature dependence of cycle life. The coefficient of $a \cdot \text{time}^x$ is replaced by the Arrhenius function to reflect the impact of the temperature on the degradation speed.

The third type of empirical model is the coupling factor model, in which the impact of both the temperature and discharge current rate is simultaneously considered. Most of coupling factor models are reshaped from the single factor empirical model with Arrhenius model such as Model 14, 15 and 17. In addition, some other coupling factor empirical models are built by the regression analysis based on the non-factor models.

To sum up, the non-factor empirical model, $a \cdot \text{time}^x$, is the common component in the empirical model. The modification and development of the empirical model by changing the coefficient and power of the non-factor model could accommodate different kinds of batteries and operating conditions.

4.2. Influence of Life Model Structure on the Normal Aging Trajectory Prediction

In this part, we compare the life model prediction accuracy for normal aging on the Dataset I and Dataset II. The battery aging data under 35 °C/1 C and 25 °C/1 C of Dataset I and battery aging data under 35 °C/1 C and 25 °C/1 C of Dataset II are as the test data to verify the extrapolation prediction accuracy of the trained life model. The other battery samples of Dataset I and Dataset II are as the train data to train the life model. The PSO algorithm is used to identify the life model parameters.

The root mean square error (RMSE) between the predicted aging curve and origin train aging data of the battery i on the train dataset is calculated by Formula (11); then, the average RMSE, max RMSE and min RMSE are calculated by Formula (12)–(14).

$$RMSE_{\text{train}, i} = \sqrt{\frac{1}{N} \cdot \sum_{n=1}^N (Q_{\text{train}, i}(n) - Q_{\text{train}, i\text{pre}}(n))^2} \quad (11)$$

$$RMSE_{\text{train}, \text{avg}} = \text{mean}(RMSE_0, RMSE_1, \dots, RMSE_k) \quad (12)$$

$$RMSE_{\text{train}, \text{max}} = \text{max}(RMSE_0, RMSE_1, \dots, RMSE_k) \quad (13)$$

$$RMSE_{\text{train}, \text{min}} = \text{min}(RMSE_0, RMSE_1, \dots, RMSE_k) \quad (14)$$

where $Q_{\text{train}, i}(n)$ is the origin aging data on the train dataset. $Q_{\text{train}, i\text{pre}}(n)$ is the predicted aging data by the life model with optimized parameters. n is the cycle number. N is the total cycle number of battery i . $RMSE_{\text{train}, i}$ is the RMSE between the predicted aging curve and origin train aging data of the battery i on the train dataset. $RMSE_{\text{train}, \text{avg}}$ is the average RMSE on the train dataset. $RMSE_{\text{train}, \text{max}}$ is the maximum RMSE on the train dataset. $RMSE_{\text{train}, \text{min}}$ is the minimum RMSE on the train dataset.

When identifying the parameters of life model, the PSO objective function is $RMSE_{\text{train}, \text{avg}}$. The particle swarm optimization algorithm minimizes the optimization target $RMSE_{\text{train}, \text{avg}}$ to obtain the life model parameters. After getting the life model parameters, we exploit the trained life model to predict the normal aging trajectory. The root mean square error ($RMSE_{\text{test}, i}$) between the predicted aging curve and origin train aging data of the battery i on the test dataset is calculated by Formula (15); then, the average RMSE on the test dataset is calculated by Formula (16)

$$RMSE_{\text{test}, i} = \sqrt{\frac{1}{N} \cdot \sum_{n=1}^N (Q_{\text{test}, i}(n) - Q_{\text{test}, i\text{pre}}(n))^2} \quad (15)$$

$$RMSE_{\text{test}, \text{avg}} = \text{mean}(RMSE_0, RMSE_1, \dots, RMSE_{k1}) \quad (16)$$

where $Q_{\text{test}, i}(n)$ is the origin aging data on the train dataset. $Q_{\text{test}, i\text{pre}}(n)$ is the predicted aging data by the life model with optimized parameters. n is the cycle number. N is the total cycle number of battery i . $RMSE_{\text{test}, \text{avg}}$ is the average RMSE on the test dataset. We adopt

the $RMSE_{test,avg}$ to evaluate the prediction performance of life model on the test dataset. We exploit the $RMSE_{train,avg}$, $RMSE_{train,max}$ and $RMSE_{train,min}$ to evaluate the prediction performance on the test dataset. The normal aging trajectory prediction results based on the non-factors model, the single factor model and the coupling factors model are shown in Figures 4–6.

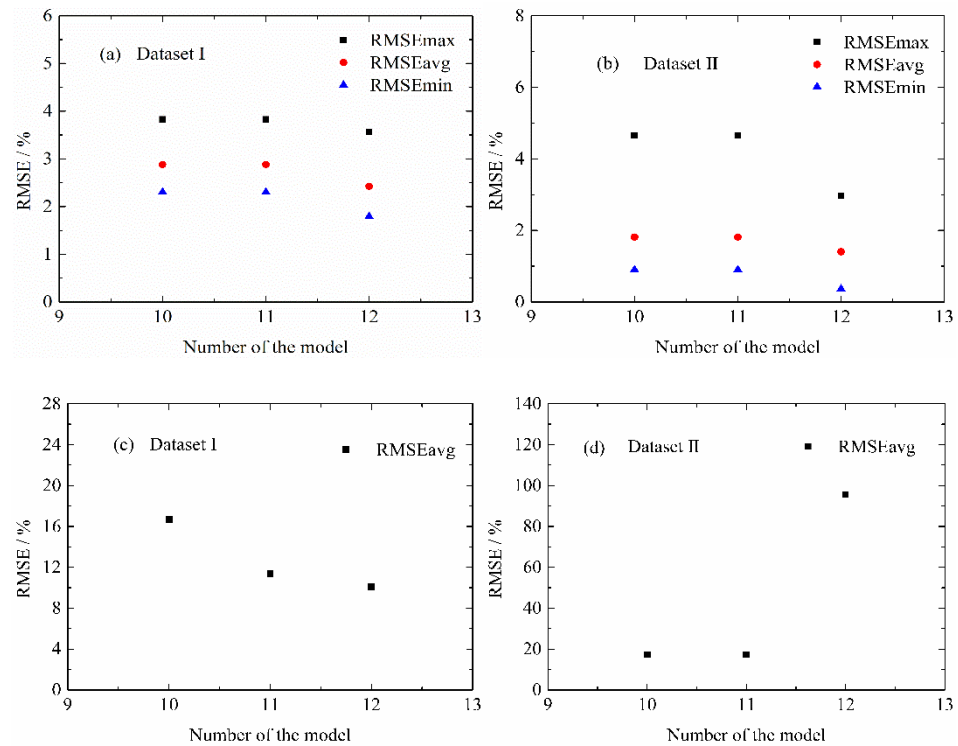


Figure 5. Prediction RMSE of the single-factor models for normal aging: (a) on the train dataset of Dataset I, (b) on the train dataset of Dataset II, (c) on the test dataset of Dataset I and (d) on the test dataset of Dataset II.

Figure 4 shows the prediction RMSE of the non-factor models for normal aging for Dataset I and II. The non-factor life models include two categories: power function and double exponential function. The basic power function life model is $a \cdot n^{0.5}$. The basic power function life model is usually rephased by adding the $a \cdot n^z$. The Model 4 is the combination of the $a \cdot time^{0.5}$ with a normal function. Model 6 has bad fitting ability and extrapolation ability at Dataset I. Although Model 6 has good fitting ability at Dataset II, its extrapolation ability is poor in Dataset II. Model 6 is proposed for a single degradation process. Model 6 has a good nonlinear fitting ability, but its parameters do not have good usability for the other conditions. In addition to Model 6, the other non-factor life models have good fitting and extrapolation behavior in both Dataset I and II. t^3 is added to Model 6 and compared to Model 4. By adding power function, the fitting accuracy and extrapolation ability of the power function can be increased, but when the power of the increased model $a \cdot time^z$ is larger than 3, the power function life model is more nonlinear and the accuracy and extrapolation ability of the power function model diminish. Above all, the power function and double exponential function are both suitable for the normal degradation of the NCM battery.

Figure 5 shows the prediction RMSE of the single-factor models for normal aging for Dataset I and II. These single-factor models consider the influence of temperature with the Arrhenius function. Single-factor Model 10, 11 and 12 can fit the normal degradation in Dataset II. The fitting error is larger in Dataset I. The extrapolation ability of the single-factor Model 10, 11 and 12 is terrible in both Dataset I and II. These single-factor models only consider the impact of the temperature, and the Arrhenius function does not reflect the

impact of the discharge current rates. Therefore, their fitting and extrapolation ability is terrible under different temperature and discharge current rates. The discharge current rate needs to be added to improve the single-factor life model.

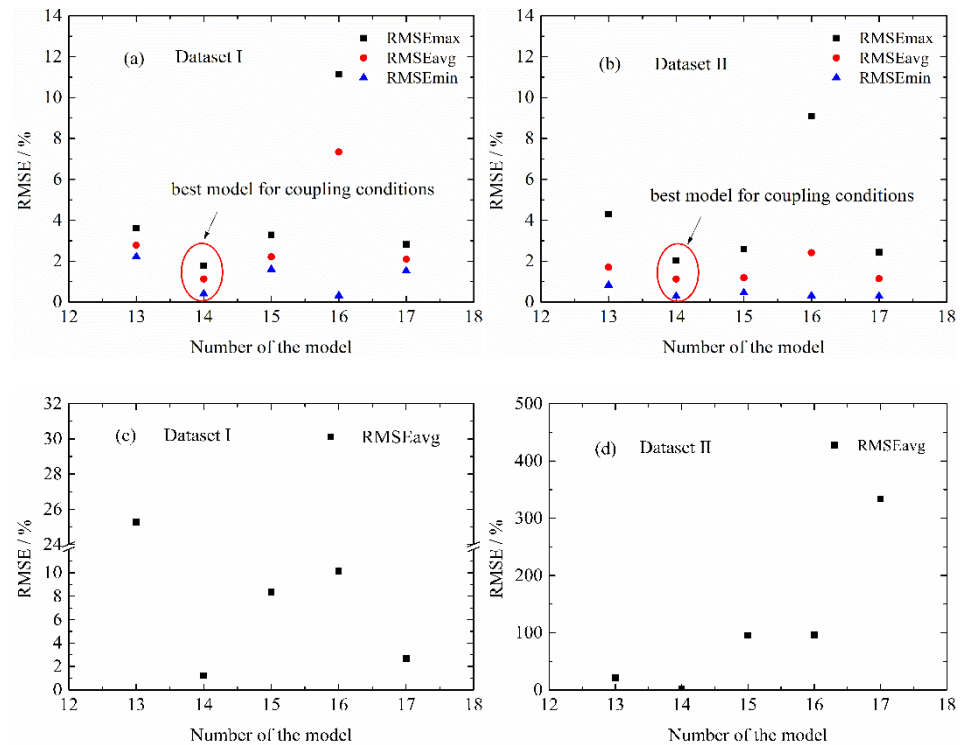


Figure 6. Prediction RMSE of the coupling-factor models for normal aging: (a) on the train dataset of Dataset I, (b) on the train dataset of Dataset II, (c) on the test dataset of Dataset I and (d) on the test dataset of Dataset II.

Figure 6 shows the prediction RMSE of the coupling-factor models for normal aging on Dataset I and II. The average RMSE of the coupling-factor Model 14 is smallest for both two datasets. Model 16 has poor fitting and extrapolation ability. Model 13, 15 and 17 have good fitting accuracy, but their extrapolation ability is not good. Model 13, 15 and 17 do not have a reasonable function for the discharge current rate. Model 14 is modified based on the single-factor model. In Model 14, both the impact of temperature and discharge current rate are taken into consideration. Model 14 improved the Arrhenius function. The pre-exponential factor of the Arrhenius function is changed to the power of the discharge current rate. In Model 14, the activation energy and discharge current ratio are linearly related. In Model 15, the activation energy and discharge current ratio are linearly related too, but their pre-exponential factor is not changed to the power of the discharge current rate. Therefore, the change of pre-exponential factor and activation energy of the Arrhenius function is the main reason for the better fitting and extrapolation ability in Model 14. By comparing the accuracy of the empirical models, the suitable model structure for the different temperature and discharge current rates has been found.

4.3. Sensitivity Analysis of the Life Model Parameters for Normal Aging Trajectory Prediction

4.3.1. Sensitivity Analysis Method

The coupling Model 14 has good prediction accuracy for both of the datasets. The Model 14 structure contains both discharge current rate and temperature. It is concluded that adding more impacts and parameters into a life model improves the prediction accuracy and robustness of life models. The influence of each model parameter on the model accuracy is different. Therefore, we exploit the parameter sensitivity analysis to find the key parameter of life models. The parameter sensitivity analysis provides a better

understanding of the model improvement. In this section, the model parameter sensitivity analysis is applied to the 17 empirical models.

The parameter sensitivity analysis MPSA method is used to analyze the influence of the parameter on the accuracy of the model. The steps of the MPSA are expressed as follows:

1. Set an appropriate variation range of the model parameter. The common values of the model parameters are calculated by the PSO algorithm. The variation range is set to be $\pm 20\%$ of the common values.
2. Generate 700 numbers with the uniform distribution within the variation range for each parameter.
3. Calculate the common output capacity retention series $Q_{b,i}$ using the empirical model with the common parameter values, where i is the condition number in the dataset. Then, calculate the distribution output capacity retention series $Q_{dis,i,n}$ using the same model with the generated parameter values, where n is the generated number. Then, the relative sensitivity criteria under different operating conditions of each model parameter can be calculated using Equation (17):

$$C_i = \sum_{n=1}^{700} (Q_{b,i} - Q_{dis,i,n})^2 / Q_{b,i} \quad (17)$$

4. Obtain the overall parameter sensitivity under all conditions. The parameter sensitivity index value S_k can be defined as the sum of the relative sensitivity criteria at various battery operating conditions, k is the parameter number and m is the number of the conditions in the Dataset I.

$$S_k = \sum_{i=1}^m C_i \quad (18)$$

4.3.2. MPSA Analysis Results and Discussion

According to the MPSA results, the parameter sensitivity index value of highly sensitive parameters is bigger than 1.0×10^2 . The highly sensitive parameter has a strong impact on the accuracy of the model. The MPSA analysis results are shown in the Table 6. The highly sensitive parameters in each model are listed.

The MPSA results indicate that the constant parameter, pre-exponential factor and index have a high impact on the output results of the empirical models. The active energy E_a has low sensitivity in the single-factor model. The accuracy of Model 14 is attributed to the improvement of the pre-exponential factor and the active energy by considering the discharge current rate. There is only a highly sensitive parameter in Model 14, 15, 16 and 17. So, the number of the highly sensitive parameters is not the main reason for the poor fitting and extrapolation ability of Model 13, 15, 16 and 17. The reason why the couple-factor life model 15, 16 and 17 is not accurate is that the form of their pre-exponential factor and index about discharge current rate are not appropriate. In order to get a more accurate model, the improvement of Model 14 can be summarized as follows: (1) reducing or improving the constant parameter, (2) improving the index and pre-exponential factor by considering both temperature and discharge current rate and (3) simplifying or improving the active energy due to its low sensitivity. In (14), the index can be improved by considering the temperature or the discharge current rate, so that the index sensitivity can be reduced.

4.4. Modified Life Model for Normal Aging Trajectory Prediction

In this section, we improved life models based on the life model comparison results and parameter sensitivity analysis results. The modified coupling-factor models based on Model 14 are listed in Table 7. Dataset I and Dataset II are used to evaluate the fitting ability and extrapolation ability of the improved models. The pre-exponential factor represents the degradation speed. The index of the model reflects the main degradation trend and mechanism. As mentioned above, the discharge current rate has a large impact on the NCM battery aging. In addition to the index of the Model 14, the calendar degradation would

be combined with Model 14. According to the MPSA analysis, the active energy could be simplified due to its low sensitivity. Model 18 improves the index of Model 14 with an exponential function that considers the discharge current rate, and its pre-exponential factor with discharge current is removed; Model 19 improves the index and the activation energy of Model 14. In Model 19, the activation energy is expressed as a function of temperature. The calendar degradation is added in Model 20 with Arrhenius model. In Model 21, only the active energy part is simplified compared to Model 14. Model 22 improves the index part with a linear function on the discharge current rate.

Table 6. Highly sensitive parameters in the empirical model parameters by MPSA analysis.

Model	Highly Sensitive Parameters
1. $Q_{loss} = 1 - (a_1 * n^{0.5} + a_2)$	a_1, a_2
2. $C = 1 - a_1 \cdot n^{0.5}$	none
3. $C = 1 - a_1 \cdot n^{0.5} - a_2 \cdot n$	none
4. $Q_{loss} = a_1 \cdot n^{0.5} + a_2 \cdot n + a_3$	none
5. $Q_{loss} = a_1 \cdot n^{0.5} + a_2 \cdot (n - N_0) + a_3$	none
6. $C = a_1 + a_2 \cdot n + a_3 \cdot n^2 + a_4 \cdot n^3$	a_2, a_3, a_4
7. $C = a_1 + a_2 \cdot n^{0.5}$	a_1, a_2
8. $Q_{loss} = 1 - (a_1 * \exp(a_2 * n) + a_3 * \exp(a_4 * n))$	a_3, a_4
9. $C = A \cdot \exp\left(\frac{n}{I_1}\right) + y_0$	A, y_0
10. $Q_{loss} = B \cdot \exp\left(\frac{-E_a}{R \cdot T}\right) \cdot n^z$	B, z
11. $Q_{loss} = B \cdot \exp\left(\frac{-E_a}{R \cdot T}\right) \cdot Ah^z$	B, z
12. $C = 1 - d_{Tref} \cdot \alpha \left(\frac{T - T_{ref}}{10}\right) \cdot n^{0.5}$	T_{ref}
13. $C = A(I, T) \cdot n^{B(I, T)}$ $A(I, T) = a \cdot \exp\left(\frac{a}{T}\right) + b \cdot I^\beta + c$ $B(I, T) = l \cdot \exp\left(\frac{\lambda}{T}\right) + m \cdot I^n + f$	a, b, c, l, m, f
14. $Q_{loss} = \alpha \cdot \exp\left(\frac{k_3 \cdot C_{rate} + k_4}{R \cdot T}\right) \cdot C_{rate}^\beta \cdot n^\eta$	η
15. $Q_{loss} = B \cdot \exp\left(\frac{a + b \cdot C_{rate}}{R \cdot T}\right) \cdot n^{0.55}$	a
16. $Q_{loss} = (a \cdot T^2 + b \cdot T + c) \cdot \exp((d \cdot T + e) \cdot I_{rate}) \cdot n$	e
17. $Q_{loss} = (a \cdot \exp(b \cdot I) + c \cdot \exp(d \cdot I)) \cdot \exp\left(\frac{e + f \cdot I}{R \cdot T}\right) \cdot Ah^{0.55}$	b

Table 7. The improved coupling-factor models based on Model 14.

Improved Models
18. $Q_{loss} = a_1 \cdot \exp\left(\frac{a_2}{R \cdot T}\right) \cdot Ah^{(C^{a_3} + a_4)}$
19. $Q_{loss} = a_1 \cdot \exp\left(\frac{a_2 \cdot T^2 + a_3}{R \cdot T}\right) \cdot Ah^{(C^{a_4} + a_5)}$
20. $Q_{loss} = a_1 \cdot \exp\left(\frac{a_2 \cdot c + a_3}{R \cdot T}\right) \cdot C^{a_4} \cdot Ah^{a_5} + a_6 \cdot \exp\left(\frac{a_7}{R \cdot T}\right) \cdot Ah^{a_8}$
21. $Q_{loss} = a_1 \cdot C^\beta \cdot \exp\left(\frac{a_2}{R \cdot T}\right) \cdot Ah^{a_3}$
22. $Q_{loss} = a_1 \cdot C^\beta \cdot \exp\left(\frac{a_2 \cdot C + a_3}{R \cdot T}\right) \cdot Ah^{a_4 \cdot C + a_5}$

The fitting and extrapolation accuracy of the improved Model 18–22 and Model 14 is shown in Figure 7. Only Model 22 has a reduced average RMSE of fitting and extrapolation ability in both Dataset I and Dataset II compared to Model 14. Model 18 has worse extrapolation accuracy than the Model 14. The pre-exponential factor with the power of discharge current rate is necessary for the couple-factor life model. Model 19 has worse extrapolation accuracy than Model 14 too. The activation energy of the Model 19 expressed with temperature is the reason for the worse extrapolation accuracy. Hence, the activation energy expressed with discharge current rate is more reasonable. The extrapolation accuracy of Model 20 is good, but its fitting ability at Dataset II is worse. The calendar degradation does not increase the fitting ability of the life model before accelerated aging.

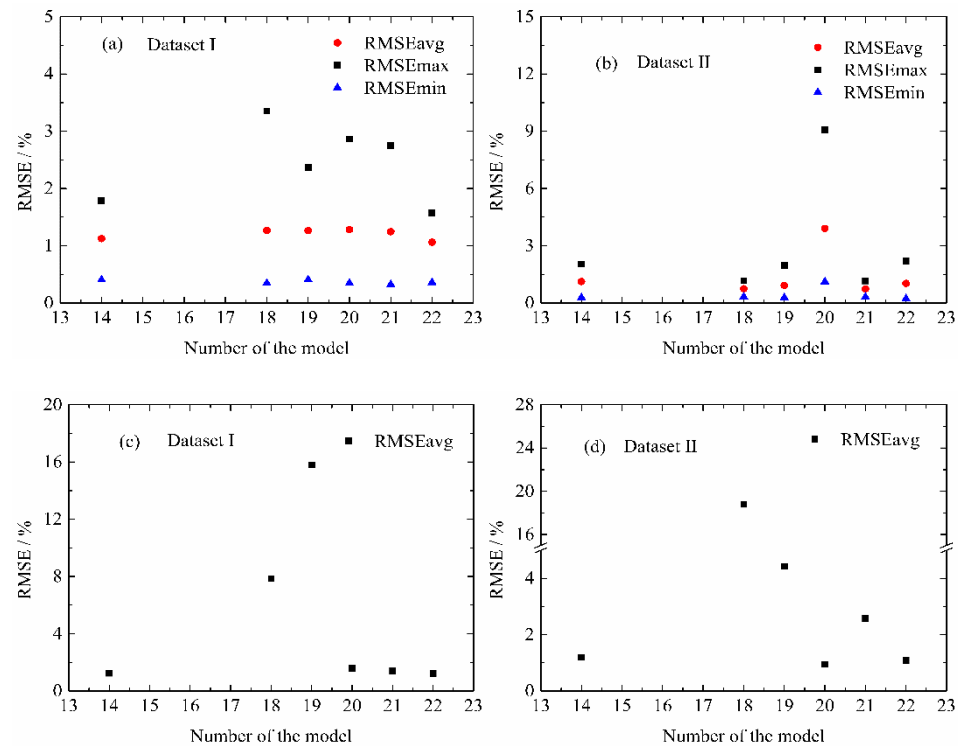


Figure 7. Prediction *RMSE* of the non-factor models for normal aging: (a) on the train dataset of Dataset I, (b) on the train dataset of Dataset II, (c) on the test dataset of Dataset I and (d) on the test dataset of Dataset II.

Above all, by improving the index of Model 14, Model 22 is the best improved life model among Model 18–22. Because of the low sensitivity of the activation energy, the active energy in Model 22 is simplified. The final improved Model 23 is as follows:

$$Q_{loss} = a_1 \cdot C^{a_2} \cdot \exp\left(\frac{a_3}{R \cdot T}\right) \cdot Ah^{a_4 \cdot C + a_5} \tag{19}$$

where *C* is the discharge current rate; *R* is the universal gas constant; *T* is the absolute temperature; *Ah* is the cumulative discharge capacity; and *a*₁, *a*₂, *a*₃, *a*₄ and *a*₅ are the model parameters.

The average *RMSE* of Model 23 for normal aging on the Dataset I and Dataset II is displayed in Table 8. Model 23 is more accurate than Model 14. The normal aging trajectory prediction results for normal aging on the test dataset of Dataset I are shown in Figure 8; the results show the modified life model has a good prediction performance for normal aging. Overall, the prediction results show that the modified life model is suitable for normal aging trajectory prediction at different temperatures and discharge current rates. Improving the index of the Model 14 and simplifying the active energy is efficient.

Table 8. The average *RMSE* for normal aging trajectory prediction by Model 14 and Model 23.

Model	Dataset I		Dataset II	
	Train Dataset	Test Dataset	Train Dataset	Test Dataset
Model 14	1.12%	1.22%	1.12%	1.19%
Model 23	1.06%	1.21%	1.02%	1.09%

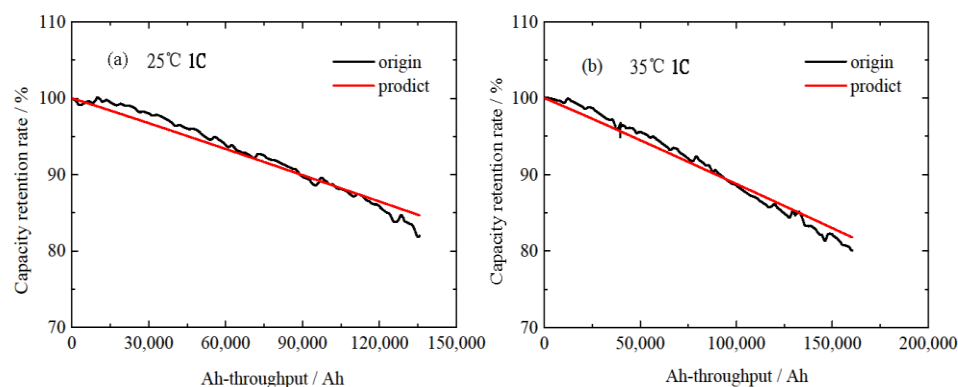


Figure 8. Accuracy validation results of the final improved model 23 under two conditions: (a) 25 °C, 1 C, and (b) 35 °C, 1 C.

All the parameters are listed in the Appendix A Table A1.

5. Conclusions

In this paper, we performed battery aging experiment and proposed a modified life model for normal aging trajectory prediction. We exploited WT to effectively remove the capacity recovery and test noise and accelerated aging decline of the battery aging trajectory. The noise reduction method based on WT can effectively extract the normal aging decline trajectory of Li-ion batteries. In this paper, the influence of life model structure and the parameters' sensitivity of the life model on the prediction accuracy of the normal aging decline trajectory are comprehensively studied. The conclusion is that establishing a suitable life model structure, reasonable simplification of life model parameters and reasonable complication of life model parameters can effectively ensure and improve the prediction accuracy of the normal aging trajectory of lithium-ion batteries. The basic structure of a life model suitable for normal aging is a power-function structure. The pre-exponential coefficients and the index of the life models are highly sensitive parameters, while the active energy part has low sensitivity. The highly sensitive parts of the life model could be improved to obtain higher accuracy. The less sensitive part of the life model could be simplified.

The modification approaches of life models for normal aging are summarized as follow: (1) the basic life model structure suitable for normal aging is the single power function structure about cycle number t : $a \cdot t^b$, a are the pre-exponential coefficients, and b is the index. (2) Modifying the pre-exponential coefficients by Arrhenius law to improve the normal aging prediction performance of the basic life model at different temperatures. (3) Modifying the pre-exponential coefficients and index by adding discharge current rate to improve the normal aging prediction performance of life model at different discharge current rates. (4) Simplifying the active energy in the Arrhenius law does not reduce the prediction accuracy of life model for normal aging. Based on the effective modification of the life model, the prediction average RMSE of the improved life model is 1.09%.

Author Contributions: Data curation, X.J.; Formal analysis, X.J.; Investigation, C.Z., L.W. and L.Z.; Methodology, X.J., C.Z., L.W. and L.Z.; Resources, W.Z.; Software, X.J.; Writing—original draft, X.J.; Writing—review & editing, L.W. All authors have read and agreed to the published version of the manuscript.

Funding: This research was funded by the National Natural Science Foundation of China: 52007006 and National Natural Science Foundation of China: 51977007.

Institutional Review Board Statement: Not applicable.

Informed Consent Statement: Not applicable.

Data Availability Statement: The NCM experiment dataset in this paper can be found at the IEEE DataPort, DOI: 10.21227/gnst-kz81.

Acknowledgments: The authors would like to thank the members of the National Active Distribution Network Technology Research Center (NANTEC), Beijing Jiaotong University for their help performing all the experiments of lithium-ion batteries mentioned in the paper.

Conflicts of Interest: The authors declare no conflict of interest.

Appendix A

This part introduces all the parameters used in each model. All the parameters are listed in the Table A1.

Table A1. All the parameters of the life model introduced in this paper.

Model	Model Parameter
1. $Q_{loss} = 1 - (a_1 * n^{0.5} + a_2)$	n is the cycle number; a_1, a_2 are the model parameters.
2. $C = 1 - a_1 * n^{0.5}$	n is the cycle number; a_1 is the model parameter.
3. $C = 1 - a_1 * n^{0.5} - a_2 * n$	n is the cycle number; a_1, a_2 are the model parameters.
4. $Q_{loss} = a_1 * n^{0.5} + a_2 * n + a_3$	n is the cycle number; a_1, a_2, a_3 are the model parameters.
5. $Q_{loss} = a_1 * n^{0.5} + a_2 * (n - N_0) + a_3$	n is the cycle number; a_1, a_2, a_3, N_0 are the model parameters.
6. $C = a_1 + a_2 * n + a_3 * n^2 + a_4 * n^3$	n is the cycle number; a_1, a_2, a_3, a_4 are the model parameters.
7. $C = a_1 + a_2 * n^{0.5}$	n is the cycle number; a_1, a_2 are the model parameters.
8. $Q_{loss} = 1 - (a_1 * \exp(a_2 * n) + a_3 * \exp(a_4 * n))$	n is the cycle number; a_1, a_2, a_3, a_4 are the model parameters.
9. $C = A * \exp\left(\frac{n}{t_1}\right) + y_0$	n is the cycle number; A, t_1, y_0 are the model parameters.
10. $Q_{loss} = B * \exp\left(\frac{-E_a}{R * T}\right) * n^z$	n is the cycle number; B and z are the model parameters; T is the absolute temperature; E_a is the active energy; and R is the universal gas constant.
11. $Q_{loss} = B * \exp\left(\frac{-E_a}{R * T}\right) * Ah^z$	Ah is the cumulative discharge capacity; B and z are the model parameters; T is the absolute temperature; E_a is the active energy; and R is the universal gas constant.
12. $C = 1 - d_{Tref} * \alpha^{\left(\frac{T - T_{ref}}{10}\right)} * n^{0.5}$	T_{ref} are model parameters; T is absolute temperature; and the T_{ref} is 40 °C in literature.
13. $C = A(I, T) * n^{B(I, T)}$ $A(I, T) = a * \exp\left(\frac{\alpha}{T}\right) + b * I^\beta + c$ $B(I, T) = l * \exp\left(\frac{\lambda}{T}\right) + m * I^n + f$	I is discharge current rate; T is absolute temperature; and $\alpha, \beta, l, \lambda, f, c$ are the model parameters.
14. $Q_{loss} = \alpha * \exp\left(\frac{k_3 * C_{rate} + k_4}{R * T}\right) * C_{rate}^\beta * n^\eta$	$\alpha \beta \eta k_3, k_4$ are model parameters; R is the universal gas constant; n is the cycle number; T is absolute temperature; and C_{rate} is the discharge current rate.
15. $Q_{loss} = B * \exp\left(\frac{a + b * C_{rate}}{R * T}\right) * n^{0.55}$	a, b, B are model parameters; R is the universal gas constant; n is the cycle number; T is absolute temperature; and C_{rate} is the discharge current rate.
16. $Q_{loss} = (a * T^2 + b * T + c) * \exp((d * T + e) * I_{rate}) * n$	T is the absolute temperature; n is the cycle number; I_{rate} is the discharge current rate; and a, b, c, d, e are the model parameters.
17. $Q_{loss} = (a * \exp(b * I) + c * \exp(d * I)) * \exp\left(\frac{e + f * I}{R * T}\right) * Ah^{0.55}$	I is the discharge current rate; R is the universal gas constant; T is the absolute temperature; Ah is the cumulative discharge capacity; and a, b, c, d, e, f are model parameters.
18. $Q_{loss} = a_1 * \exp\left(\frac{a_2}{R * T}\right) * Ah^{C^{a_3 + a_4}}$	C is the discharge current rate; R is the universal gas constant; T is the absolute temperature; Ah is the cumulative discharge capacity; a_1, a_2, a_3, a_4 are the model parameters; $-a_2$ represents the active energy;
19. $Q_{loss} = a_1 * \exp\left(\frac{a_2 * T^2 + a_3}{R * T}\right) * Ah^{(C^{a_4 + a_5})}$	R is the universal gas constant; T is the absolute temperature; Ah is the cumulative discharge capacity; and a_1, a_2, a_3, a_4, a_5 are the model parameters.

Table A1. Cont.

Model	Model Parameter
20. $Q_{loss} = a_1 \cdot \exp\left(\frac{a_2 \cdot C + a_3}{R \cdot T}\right) \cdot C^{a_4} \cdot Ah^{a_5} + a_6 \cdot \exp\left(\frac{a_7}{R \cdot T}\right) \cdot Ah^{a_8}$	C is the discharge current rate; R is the universal gas constant; T is the absolute temperature; Ah is the cumulative discharge capacity; and $a_1, a_2, a_3, a_4, a_5, a_6, a_7, a_8$ are the model parameters.
21. $Q_{loss} = a_1 \cdot C^\beta \cdot \exp\left(\frac{a_2}{R \cdot T}\right) \cdot Ah^{a_3}$	C is the discharge current rate; R is the universal gas constant; T is the absolute temperature; Ah is the cumulative discharge capacity; a_1, a_2, a_3, β are the model parameters; $-a_2$ represents the active energy;
22. $Q_{loss} = a_1 \cdot C^\beta \cdot \exp\left(\frac{a_2 \cdot C + a_3}{R \cdot T}\right) \cdot Ah^{(a_4 \cdot C + a_5)}$	C is the discharge current rate; R is the universal gas constant; T is the absolute temperature; Ah is the cumulative discharge capacity; and $a_1, a_2, a_3, a_4, a_5, \beta$ are the model parameters.
23. $Q_{loss} = a_1 \cdot C^{a_2} \cdot \exp\left(\frac{a_3}{R \cdot T}\right) \cdot Ah^{(a_4 \cdot C + a_5)}$	C is the discharge current rate; R is the universal gas constant; T is the absolute temperature; Ah is the cumulative discharge capacity; and a_1, a_2, a_3, a_4, a_5 are the model parameters. $-a_3$ represents the active energy

References

- Gao, Y.; Jiang, J.; Zhang, C.; Zhang, W.; Jiang, Y. Aging Mechanisms Under Different State-Of-Charge Ranges and the Multi-Indicators System of State-Of-Health for Lithium-Ion Battery with Li(NiMnCo)O₂ Cathode. *J. Power Sources* **2018**, *400*, 641–651. [\[CrossRef\]](#)
- Han, X.; Meng, Q.; Sun, T.; Sun, J. Preparation and Electrochemical Characterization of Single-Crystalline Spherical LiNi_{1/3}Co_{1/3}Mn_{1/3}O₂ Powders Cathode Material for Li-ion Batteries. *J. Power Sources* **2010**, *195*, 3047–3052. [\[CrossRef\]](#)
- Barré, A.; Deguilhem, B.; Grolleau, S.; Gérard, M.; Suard, F.; Riu, D. A Review on Lithium-Ion Battery Aging Mechanisms and Estimations for Automotive Applications. *J. Power Sources* **2013**, *241*, 680–689. [\[CrossRef\]](#)
- Han, X.; Lu, L.; Zheng, Y.; Feng, X.; Li, Z.; Li, J.; Ouyang, M. A Review on the Key Issues of the Lithium Ion Battery Degradation Among the Whole Life Cycle. *eTransportation* **2019**, *1*, 100005. [\[CrossRef\]](#)
- Jalkanen, K.; Karppinen, J.; Skogström, L.; Laurila, T.; Nisula, M.; Vuorilehto, K. Cycle Aging of Commercial NMC/graphite Pouch Cells at Different Temperatures. *Appl. Energy* **2015**, *154*, 160–172. [\[CrossRef\]](#)
- Bitzerand, B.; Gruhle, A. A New Method for Detecting Lithium Plating by Measuring the Cell Thickness. *J. Power Sources* **2014**, *262*, 297–302. [\[CrossRef\]](#)
- Sarasketa-Zabala, E.; Gandiaga, I.; Martinez-Laserna, E.; Rodriguez-Martinez, L.M.; Villarreal, I. Cycle Aging Analysis of a LiFePO₄/graphite Cell with Dynamic Model Validations: Towards Realistic Lifetime Predictions. *J. Power Sources* **2015**, *275*, 573–587. [\[CrossRef\]](#)
- Wu, L.; Fuand, X.; Guan, Y. Review of the Remaining Useful Life Prognostics of Vehicle Lithium-Ion Batteries Using Data-Driven Methodologies. *Appl. Sci.* **2016**, *6*, 166. [\[CrossRef\]](#)
- Jafari, M.; Khan, K.; Gauchia, L. Deterministic Models of Li-ion Battery Aging: It is a Matter of Scale. *J. Energy Storage* **2018**, *20*, 67–77. [\[CrossRef\]](#)
- Ahmadian, A.; Sedghi, M.; Elkamel, A.; Fowler, M.; Golkar, M.A. Plug-In Electric Vehicle Batteries Degradation Modeling for Smart Grid Studies: Review, Assessment and Conceptual Framework. *Renew. Sustain. Energy Rev.* **2018**, *81*, 2609–2624. [\[CrossRef\]](#)
- Nuhic, A.; Terzimehic, T.; Soczka-Guth, T.; Buchholz, M.; Dietmayer, K. Health Diagnosis and Remaining Useful Life Prognostics of Lithium-Ion Batteries Using Data-Driven Methods. *J. Power Sources* **2013**, *239*, 680–688. [\[CrossRef\]](#)
- Hu, X.; Jiang, J.; Cao, D.; Egardt, B. Battery Health Prognosis for Electric Vehicles Using Sample Entropy and Sparse Bayesian Predictive Modeling. *IEEE Trans. Ind. Electron.* **2015**, *63*, 2645–2656. [\[CrossRef\]](#)
- Zhang, Y.; Xiong, R.; He, H.; Pecht, M.G. Long Short-Term Memory Recurrent Neural Network for Remaining Useful Life Prediction of Lithium-Ion Batteries. *IEEE Trans. Veh. Technol.* **2018**, *67*, 5695–5705. [\[CrossRef\]](#)
- Severson, K.A.; Attia, P.M.; Jin, N.; Perkins, N.; Jiang, B.; Yang, Z.; Chen, M.H.; Aykol, M.; Herring, P.K.; Fraggadakis, D.; et al. Data-Driven Prediction of Battery Cycle Life Before Capacity Degradation. *Nat. Energy* **2019**, *4*, 383–391. [\[CrossRef\]](#)
- Hu, C.; Jain, G.; Tamirisa, P.; Gorka, T. Method for Estimating Capacity and Predicting Remaining Useful Life of Lithium-Ion Battery. *Appl. Energy* **2014**, *126*, 182–189. [\[CrossRef\]](#)
- Bloom, I.; Cole, B.W.; Sohn, J.J.; Jones, S.A.; Polzin, E.G.; Battaglia, V.S.; Henriksen, G.L.; Motloch, C.; Richardson, R.; Unkelhaeuser, T.; et al. An Accelerated Calendar and Cycle Life Study of Li-ion Cells. *J. Power Sources* **2001**, *101*, 238–247. [\[CrossRef\]](#)
- Käbitz, S.; Gerschler, J.B.; Ecker, M.; Yurdagel, Y.; Emmermacher, B.; André, D.; Mitschand, T.; Sauer, D.U. Cycle and Calendar Life Study of a Graphite | LiNi_{1/3}Mn_{1/3}Co_{1/3}O₂ Li-ion High Energy System. Part a: Full Cell Characterization. *J. Power Sources* **2013**, *239*, 572–583. [\[CrossRef\]](#)
- Lee, Y.J.; Choi, H.Y.; Ha, C.W.; Yu, J.H.; Hwang, M.J.; Doh, C.H.; Choi, J.H. Cycle Life Modeling and the Capacity Fading Mechanisms in a graphite/LiNi_{0.6}Co_{0.2}Mn_{0.2}O₂ Cell. *J. Appl. Electrochem.* **2015**, *45*, 419–426. [\[CrossRef\]](#)

19. He, W.; Williard, N.; Osterman, M.; Pecht, M. Prognostics of Lithium-Ion Batteries Based On Dempster–Shafer Theory and the Bayesian Monte Carlo Method. *J. Power Sources* **2011**, *196*, 10314–10321. [[CrossRef](#)]
20. Unoand, M.; Tanaka, K. Accelerated Charge–Discharge Cycling Test and Cycle Life Prediction Model for Supercapacitors in Alternative Battery Applications. *IEEE Trans. Ind. Electron.* **2012**, *59*, 4704–4712.
21. Cordoba-Arenas, A.; Onori, S.; Guezennec, Y.; Rizzoni, G. Capacity and Power Fade Cycle-Life Model for Plug-In Hybrid Electric Vehicle Lithium-Ion Battery Cells Containing Blended Spinel and Layered-Oxide Positive Electrodes. *J. Power Sources* **2015**, *278*, 473–483. [[CrossRef](#)]
22. Wang, J.; Purewal, J.; Liu, P.; Hicks-Garner, J.; Soukazian, S.; Sherman, E.; Sorenson, A.; Vu, L.; Tataria, H.; Verbrugge, M.W. Degradation of Lithium Ion Batteries Employing Graphite Negatives and Nickel–Cobalt–Manganese Oxide + Spinel Manganese Oxide Positives: Part 1, Aging Mechanisms and Life Estimation. *J. Power Sources* **2014**, *269*, 937–948. [[CrossRef](#)]
23. Schmalstieg, J.; Käbitz, S.; Ecker, M.; Sauer, D.U. A Holistic Aging Model for Li(NiMnCo)O₂ Based 18650 Lithium-Ion Batteries. *J. Power Sources* **2014**, *257*, 325–334. [[CrossRef](#)]
24. Diao, W.; Saxenaand, S.; Pecht, M. Accelerated Cycle Life Testing and Capacity Degradation Modeling of LiCoO₂-graphite Cells. *J. Power Sources* **2019**, *435*, 226830. [[CrossRef](#)]
25. Cong, X.; Zhang, C.; Jiang, J.; Zhang, W.; Jiang, Y. A Hybrid Method for the Prediction of the Remaining Useful Life of Lithium-Ion Batteries with Accelerated Capacity Degradation. *IEEE Trans. Veh. Technol.* **2020**, *69*, 12775–12785. [[CrossRef](#)]
26. Tröltzsch, U.; Kanoun, O.; Tränkler, H.R. Characterizing Aging Effects of Lithium Ion Batteries by Impedance Spectroscopy. *Electrochim. Acta* **2006**, *51*, 1664–1672. [[CrossRef](#)]
27. Zhangand, Q.; White, R.E. Capacity Fade Analysis of a Lithium Ion Cell. *J. Power Sources* **2008**, *179*, 793–798. [[CrossRef](#)]
28. Burns, J.C.; Jain, G.; Smith, A.J.; Eberman, K.W.; Scott, E.; Gardner, J.P.; Dahn, J.R. Dahn Evaluation of Effects of Additives in Wound Li-Ion Cells through High Precision Coulometry. *J. Electrochem. Soc.* **2011**, *158*, A255. [[CrossRef](#)]
29. Yang, X.G.; Leng, Y.; Zhang, G.; Ge, S.; Wang, C.Y. Modeling of Lithium Plating Induced Aging of Lithium-Ion Batteries: Transition from Linear to Nonlinear Aging. *J. Power Sources* **2017**, *360*, 28–40. [[CrossRef](#)]
30. Burrell, R.M.; Zulke, A.A.; Keil, P.; Hoster, H. Communication—Identifying and Managing Reversible Capacity Losses that Falsify Cycle Aging Tests of Lithium-Ion Cells. *J. Electrochem. Soc.* **2020**, *167*, 130544. [[CrossRef](#)]
31. Konishi, H.; Yoshikawa, M.; Hirano, T.; Hidaka, K. Evaluation of Thermal Stability in Li_{0.2}Ni_xMn_{(1-x)/2}Co_{(1-x)/2}O₂ (X = 1/3, 0.6, and 0.8) through X-ray Absorption Fine Structure. *J. Power Sources* **2014**, *254*, 338–344. [[CrossRef](#)]
32. Noh, H.J.; Youn, S.; Yoon, C.S.; Sun, Y.K. Comparison of the Structural and Electrochemical Properties of Layered Li[Ni_xCo_yMn_z]O₂ (X = 1/3, 0.5, 0.6, 0.7, 0.8 and 0.85) Cathode Material for Lithium-Ion Batteries. *J. Power Sources* **2013**, *233*, 121–130. [[CrossRef](#)]
33. Huang, Z.D.; Liu, X.M.; Zhang, B.; Oh, S.W.; Ma, P.C.; Kim, J.K. LiNi_{1/3}Co_{1/3}Mn_{1/3}O₂ with a Novel One-Dimensional Porous Structure: A High-Power Cathode Material for Rechargeable Li-ion Batteries. *Scr. Mater.* **2011**, *64*, 122–125. [[CrossRef](#)]
34. Eddahech, A.; Briatand, O.; Vinassa, J. Lithium-Ion Battery Performance Improvement Based On Capacity Recovery Exploitation. *Electrochim. Acta* **2013**, *114*, 750–757. [[CrossRef](#)]
35. Zhou, D.; Zhang, K.; Ravey, A.; Gao, F.; Miraoui, A. Parameter Sensitivity Analysis for Fractional-Order Modeling of Lithium-Ion Batteries. *Energies* **2016**, *9*, 123. [[CrossRef](#)]
36. Zhang, Z.; Si, X.; Huand, C.; Pecht, M.G. A Prognostic Model for Stochastic Degrading Systems with State Recovery: Application to Li-Ion Batteries. *IEEE Trans. Reliab.* **2017**, *66*, 1293–1308. [[CrossRef](#)]
37. Wang, F.; Fan, B.; Liu, S.; Qian, G.; Huang, X.; Han, S. Attenuation Test and Duplication of Power Battery’s Cycle Life. *J. Automot. Saf. Energy* **2012**, *3*, 71–76.
38. Wei, S. *Research on Lifespan Factors and Test Methods of Traction Lithium-Ion Batteries*; Beijing Jiaotong University: Beijing, China, 2014.
39. Yafei, L. *Study on Life Estimation and Optimization of Lithium-Ion Power Battery for Extended Range Electric Vehicle*; South China University of Technology: Guangzhou, China, 2015.
40. Lifuand, L.; Dongyu, Z. Cycle Life Prediction Method of Lithium Batteries Basedon Morphology and Properties. *J. South China Univ. Technol.* **2018**, *4*, 7–13.
41. Li, H.L.; Su, J.R. Cycle-Life Prediction Model Studies of Lithium-Ion Batteries. *Chin. J. Power Sources* **2008**, *32*, 242–246.
42. Wang, J.; Liu, P.; Hicks-Garner, J.; Sherman, E.; Soukiaizian, S.; Verbrugge, M.; Tataria, H.; Musser, J.; Finamore, P. Cycle-Life Model for graphite-LiFePO₄ Cells. *J. Power Sources* **2011**, *196*, 3942–3948. [[CrossRef](#)]
43. Yutao, L.; Feng, W.; Hao, Y.; Xiutian, L. A Study on the Driving-cycle-based Life Model for LiFePO₄ Battery. *Automot. Eng.* **2015**, *37*, 881–885.